Soft Matter

Effect of Matrix Heterogeneity on Cell Mechanosensing

Journal:	*Soft Matter*
Manuscript ID	SM-ART-02-2021-000312.R1
Article Type:	Paper
Date Submitted by the Author:	22-May-2021

Complete List of Authors:	Proestaki, Maria; University of Wisconsin-Madison, Department of Engineering Physics Burkel, Brian; University of Wisconsin-Madison, Department of Cell and Regenerative Biology Galles, Emmett; University of Wisconsin-Madison, Department of Engineering Physics Ponik, Suzanne; University of Wisconsin-Madison, Department of Cell and Regenerative Biology; University of Wisconsin-Madison, Carbone Cancer Center Notbohm, Jacob; University of Wisconsin-Madison, Department of Engineering Physics; University of Wisconsin-Madison, Carbone Cancer Center

Effect of Matrix Heterogeneity on Cell Mechanosensing

Maria Proestaki[a], Brian M. Burkel[b], Emmett E. Galles[a], Suzanne M. Ponik[b,c], Jacob Notbohm[a,c]

[a] Department of Engineering Physics, University of Wisconsin–Madison, Madison, WI, USA

[b] Department of Cell and Regenerative Biology, University of Wisconsin School of Medicine and Public Health, Madison, WI, USA

[c] University of Wisconsin Carbone Cancer Center, Madison, WI, USA

Abstract

Cells sense mechanical signals within the extracellular matrix, the most familiar being stiffness, but matrix stiffness cannot be simply described by a single value. Randomness in matrix structure causes stiffness at the scale of a cell to vary by more than an order of magnitude. Additionally, the extracellular matrix contains ducts, blood vessels, and, in cancer or fibrosis, regions with abnormally high stiffness. These different features could alter the stiffness sensed by a cell, but it is unclear whether the change in stiffness is large enough to overcome the noise caused by heterogeneity due to the random fibrous structure. Here we used a combination of experiments and modeling to determine the extent to which matrix heterogeneity disrupts the potential for cell sensing of a locally stiff feature in the matrix. Results showed that, at the scale of a single cell, spatial heterogeneity in local stiffness was larger than the increase in stiffness due to a stiff feature. The heterogeneity was reduced only for large length scales compared to the fiber length. Experiments verified this conclusion, showing spheroids of cells, which were large compared to the average fiber length, spreading preferentially toward stiff inclusions. Hence, the propagation of mechanical cues through the matrix depends on length scale, with single cells able to sense only the stiffness of the nearby fibers and multicellular structures, such as tumors, also sensing the stiffness of distant matrix features.

Introduction

Mechanical cues from the extracellular matrix (ECM), including stiffness and forces propagating through it, affect cell functions ranging from migration to contraction to gene expression.[1–4] A fundamental challenge in relating mechanics to cell function is that the ECM is mechanically heterogeneous. Even relatively simple gels made of collagen or fibrin exhibit spatial variability in local stiffness ranging from factors of $\sim$3 to more than an order of magnitude depending on the size of the stiffness probe relative to the length of the fibers.[5–9] When cells are added to such fibrous gels, the heterogeneities are amplified, with stiffness varying by more than two orders of magnitude.[10,11]

Real tissues are structurally more complex than gels of collagen, with ducts and vessels present. Diseased tissues may also contain features of abnormally high stiffness, such as fibrotic scars, stiff arterial walls, and tumors. These structural features cause mechanical heterogeneities. Indeed, indentation by atomic force microscopy on real tissues has shown stiffness to vary by up to two orders of magnitude, with the greater variation in fibrotic tissues compared to benign.[12–16] These studies have given important information about the range of stiffness in a cell's microenvironment. Complete understanding of the relationships between structural features and stiffness is lacking, however, because mechanical cues propagate over space. In fi-

brous materials, locally-applied displacements propagate over a large distance due to nonlinearity caused by the fibrous structure.[17–20] Under some conditions, the long range displacement propagation enables cells to sense and respond to stiff features located several cell lengths away.[21,22] The distance of cell sensing depends strongly on the fiber structure near to the cells. For example, aligned bands of fibers form between cells or multicellular spheroids at distances greater than an order of magnitude larger than the size of the cell or spheroid.[18,23–25] These aligned fiber bands have been the topic of much recent research showing that they result from an instability caused fiber buckling[18,26,27] with additional contributions from plastic deformation.[28,29] Less is known, however, about how mechanical cues propagate through nominally isotropic fibrous materials that lack aligned fiber bands. The few prior studies on this topic have established that propagation of forces and displacements through a fibrous matrix is highly heterogeneous.[30,31] The question of the mechanics of nominally isotropic matrices is important, because fibers in the ECM have random orientation in benign tissue and even in early stages of disease.[15,32–34] Hence, the prior research on aligned fiber bands may be informative for late stages of disease but not necessarily for maintenance of benign tissue.

Here we studied how mechanical cues propagate through a matrix of fibers with random orientation. The cues we investigated were stiff inclusions in the matrix, which provide a first step toward mimicking real tissue structures like ducts, blood vessels, or tumors. Our study began with experiments that quantified how displacement fields caused by a contracting particle were altered by a stiff inclusion. The experimental data were used to verify that a fiber network model captured the same trends. We then used the model to predict the stiffness that would be sensed by contracting in the fiber network at different distances from the stiff inclusion. Model results informed experiments with cell spheroids embedded in collagen matrices that demonstrated spheroid spreading due to migrating cells was affected by the presence of a nearby stiff inclusion.

Methods

Sample Preparation and Imaging of Mouse ECM

Mice were maintained and bred under the oversight and ethical approval of the University of Wisconsin Animal Use and Care Committee (approved protocol number M005840-R01A01). Mixed background FVB/B6 mice expressing the MMTV-PyMT transgene were raised for 8-10 weeks until a palpable mass was detected. Tumors and glands were then harvested and imaged *ex vivo*. Briefly, the glands or tumors were excised, washed with phosphate buffered saline (PBS), and placed on a glass bottom dish to be imaged immediately after harvest. To obtain a transverse view of collagen organization, glands were cross sectioned with a vibratome to obtain 300 μm thick sections. The tumors or sections were then imaged with a Bruker Ultima Multiphoton Microscope equipped with PrairieView 5.4 software, a Zeiss 20× water immersion numerical aperture 1.0 objective and Hamamatsu R3788 multi-alkali photomultipliers. A Coherent Chameleon Ti-Sapphire laser was tuned to 890 nm to simultaneously acquire both second harmonic generation (450/40) and flavin adenine dinucleotide autofluorescence (585/65) or tuned to 780 nm to collect nicotinamide adenine dinucleotide autofluorescence (450/40).

Experiments with Contracting Particles and Stiff Inclusions

Preparation of Collagen Matrices

Particles of poly(N-isopropylacrylamide) (PNIPAAm) of radius $\sim$70 μm were made as described in our prior work.[20] These particles contract when heated allowing us to apply controlled displacements at the microscale mimicking cell-induced displacements. In a prior study, we verified that temperature change did not affect the collagen matrix.[20] To induce displacements in matrices of fibrous collagen, PNIPAAm particles were covalently attached to collagen fibers. Briefly, the PNIPAAm particles were treated with sulfo-SANPAH (1 mg/mL final concentration, Proteochem) and exposed to ultraviolet light for 10 min. After exposure, the treated particles were washed with 0.05 M HEPES and 1$\times$ PBS. The particles were then mixed with Alexa-488 labeled, neutralized rat tail collagen I (Corning, Inc.), with a final collagen concentration of 2 mg/mL as previously described.[20] Stiff rectangular inclusions made of poly(dimethylsiloxane) (PDMS) were included in the collagen gels. To functionalize the PDMS rectangles for collagen bonding, they were incubated in 1% poly(ethyleneimine) (Sigma) for 1 hr and then transferred to 0.1% gluteraldehyde (Sigma) for 30 minutes. The treated PDMS rectangles were then washed 4-5 times with PBS and placed on the bottom of a 20 mm glass bottom dish. The neutralized solution of collagen and PNIPAAm was then added to the PDMS rectangles and allowed to polymerize at 25°C for 1 hr prior to imaging. 1 mL of PBS was added to the polymerized gels prior to imaging to prevent dehydration. In this manuscript we refer to the collagen fiber length, which we define to be the distance between nodes that connect multiple fiber branches. Following our previous study that measured fiber length in collagen matrices polymerized under similar conditions,[31] the fiber length l_f was estimated to be $\approx$ 35 μm, which gave a ratio of PNIPAAm particle radius to fiber length of $R/l_f \approx 2$.

Microscopy and Image Correlation

Imaging of PNIPAAm particles relative to stiff inclusions was performed using a Bruker Ultima Multiphoton Microscope equipped with a Coherent Chameleon Ti-Sapphire laser and Hamamatsu R3788 multi-alkali photomultipliers. To visualize the Alexa-488 collagen fibers, the laser was tuned to 890 nm and collected with a 20$\times$ numerical aperture 0.45 objective (Nikon) using a 520/40 nm filter cube. The PNIPAAm microspheres were contracted by elevating the temperature of the system using an OkoLab stage top incubator while imaging. After elevating the temperature to induce displacements, collagen gels with their embedded particles were allowed to equilibrate for approximately 10 min before image acquisition.

As in our prior work,[20,31] displacement fields were computed with Fast Iterative Digital Image Correlation,[35] using a subset size of 48 $\times$ 48 pix and a subset spacing of 12 pix (14 μm). The center of each particle was identified, and the radial component of displacement u_r was fit to the function $u_r = Ar^{-n}$ to determine the displacement decay rate n, which quantifies how quickly displacements decay over space.[18,20,36] The decay rate n was determined along different radial paths in directions away from and towards the stiff inclusion. 95% confidence intervals of the ratio of n away from and towards the inclusion were computed by bootstrap analysis in Matlab using 10^4 bootstrap samples.

Fiber Network Modeling

Fiber Network Generation

Fiber networks were generated on computer using methods designed to match the structure of real collagen matrices.[36–38] Prior studies have demonstrated that this algorithm creates fiber networks with mechanical properties that match experimental data[37,38] and that mechanical heterogeneity in these networks is largely similar to heterogeneity in networks produced using other network generation algorithms.[31] In brief, the algorithm randomly placed nodes within a two-dimensional domain until a desired nodal density (nodes per unit area) was reached. Each node was assigned a connectivity, defined as the number of fibers meeting at that node. Consistent with experimental observations,[37,38] the average connectivity was chosen to be 3.4. Fibers were then connected to nodes until 98% of the nodes had the correct connectivity. Next, nodes were moved and fibers connecting nodes were swapped until the network had a desired distribution of fiber lengths. Lastly, nodes were moved once again to change the angles of fibers to match those observed experimentally in images of collagen matrices.[36] The average fiber length l_f was used as the length scale in the simulations. Fiber networks were generated at two different densities, where density was defined as the average number of fibers per square area of size l_f^2. Five different fiber networks were generated with a fiber density of 7.5 l_f^{-2}, which was chosen based on the network density that gave the best qualitative match in displacement fields between experiments and model. To evaluate the effect of fiber density, five more fiber networks were generated with a higher density of 15 l_f^{-2}. Unless otherwise stated, results shown correspond to networks of the lower fiber density, 7.5 l_f^{-2}. Note that our fiber network generation algorithm produces locations where fibers cross without connecting, which is consistent with images of real networks made of collagen fibers,[31,39] and explains why fiber densities can be significantly larger than unity.

Fiber Mechanical Properties

Each fiber within the network was modeled as a 2-node linear Timoshenko beam with axial, bending and shear stiffness, k_a, k_b, and k_s, respectively. The ratio $\kappa = k_b/k_a$ defines the dimensionless ratio of bending to axial stiffness. The order of magnitude of κ can be determined by assuming the fibers to be homogeneous rods with circular cross section, in which case κ is proportional to the volume fraction of the fiber network.[40–42] Based on this scaling, κ has a value in the range of 10^{-4}–10^{-3}, which gives a good match between data from experiments and fiber network models.[40–42] Next, the ratio $\kappa_s = k_s/k_a = G_f/E_f$ defines the dimensionless ratio of shear to axial stiffness, where G_f and E_f are the fiber's shear and Young's moduli. All simulations used $\kappa = 10^{-3}$ and $\kappa_s = 0.5$.

Boundary Conditions and Finite Element Solver

Two different boundary conditions were used, a contracting circle and a contracting dipole. For the contracting circle, fiber networks were cropped into an annulus. The inner radius was R, initially chosen such that the ratio R/l_f equaled 2, which matched the experiments with PNIPAAm particles as stated above. Where stated in the text, a larger value of R/l_f of 10 was chosen to investigate effects of changing R/l_f. Nodes inside the annulus were filled with triangular 3-node continuum elements that underwent isotropic thermal contraction. Young's modulus of the contracting circle was chosen such that circle's actual strain was approximately half the thermal strain. The outer radius of the fiber network was $20R$, making the results minimally affected by the outer boundary.[36] Lastly, a rectangular region having fixed nodes was added to represent a stiff inclusion in the fiber network. The stiff inclusion was located at various dimension-

less distances d/R from the contracting circle ranging from 0.1 to 4. The stiff inclusion had a height of $20R$ and extended outward from the contracting circle to the boundary of the fiber network. Additionally, some simulations were run with no stiff inclusion, to study mechanics of the nominally homogeneous fiber network.

For contracting dipoles, a circular fiber network was used. The dipole was modeled as a 2-node truss element of size $2R$ that underwent thermal contraction. The stiffness of the dipole truss element was 6 orders of magnitude greater than the axial stiffness of the fibers, which ensured that the thermal strain of the dipole was equal to its actual strain. The radius of the fiber network was $20R$ to match the simulations with contracting circles. Lastly, a stiff inclusion was modeled by fixing nodes a distance d/R away from the dipole as described for the simulations with contracting circles. Simulations were performed with dipoles oriented both parallel and perpendicular to the stiff inclusion. Upon completion of the simulation, the internal force in the dipole was extracted and made dimensionless by dividing by $l_f^2 E_f$; the dipole displacement was made dimensionless by dividing by initial length. The ratio of dimensionless force and displacement gave a dimensionless stiffness sensed by the dipole.

The finite element software Abaqus 6.16 was used to solve the model. As large displacements were produced, the implicit dynamic quasistatic solver was used.

Relationship between Circle Contraction and Local Modulus

In the fiber network model, the radial strain of the contracting circle, together with its modulus and thermal strain, can be used to determine the apparent modulus at the location of the contracting circle. In a prior study,[8] we used a nonlinear constitutive model for fibrous materials[43] to derive the relationship in three dimensions. Here, we derive the relationship in two dimensions, to match the fiber network model. The constitutive model we use has three elastic constants, two moduli as in linear elasticity and a compression weakening factor ρ defined as the ratio of stiffness in compression and tension, $0 \leq \rho \leq 1$. From Eq. 3.11 of ref.[43], radial displacements u_r^M and stresses σ_{rr}^M caused by a contracting circle of radius R in an infinite, two-dimensional matrix under conditions of plane strain are given by

$$u_r^M = -\varepsilon R \left(\frac{R}{r}\right)^{\sqrt{\rho}} \tag{1}$$

and

$$\sigma_{rr}^M = \frac{u_0}{R} \frac{\sqrt{\rho}(\alpha^2 - \beta^2)}{\alpha + \beta\sqrt{\rho}} \left(\frac{R}{r}\right)^{\sqrt{\rho}+1}, \tag{2}$$

where r is the radial position, ε is the magnitude of contractile strain of the circle, and α and β are elastic constants, $\alpha = E^M(1-\nu^M)/[(1+\nu^M)(1-2\nu^M)]$ and $\beta = E^M\nu^M/[(1+\nu^M)(1-2\nu^M)]$, with E^M and ν^M being Young's modulus and Poisson's ratio of the matrix.

We relate Eqs. 1 & 2, which apply for the matrix, to the radial displacement and stress of the contracting circle, u_r^C and σ_{rr}^C. In the model, the circle undergoes a thermal strain ε_T, so the total strain is given by $\varepsilon = \varepsilon_M + \varepsilon_T$, with ε_M being the mechanical strain. We note that both the thermal strain and the mechanical strain inside the contracting circle are constant. The radial displacement of the contracting circle is determined from the total strain ε according to

$$u_r^C = \varepsilon r \tag{3}$$

As the contracting circle in the fiber network model is linearly elastic, the radial stress is related to the mechanical strain using equations of linear elasticity in plane strain,

$$\sigma_{rr}^{C} = 2\left(\lambda^{C} + \mu^{C}\right)\varepsilon_{M}, \tag{4}$$

where λ^{C} and μ^{C} are Lamé and shear moduli of the contracting circle. Lastly, using $\varepsilon_{M} = \varepsilon - \varepsilon_{T}$, we have

$$\sigma_{rr}^{C} = 2\left(\lambda^{C} + \mu^{C}\right)\left(\varepsilon - \varepsilon_{T}\right). \tag{5}$$

Applying the two boundary conditions $u_{r}^{M}(r=R) = u_{r}^{C}(r=R)$ and $\sigma_{rr}^{M}(r=R) = \sigma_{rr}^{C}(r=R)$ and simplifying gives

$$E^{M} = \frac{1}{g(\nu,\rho)}\left(\lambda^{C} + \mu^{C}\right)\left(\frac{\varepsilon_{T}}{\varepsilon} - 1\right), \tag{6}$$

where $g(\nu,\rho)$ is given by

$$g(\nu,\rho) = \frac{1}{2}\frac{\sqrt{\rho}}{1 + (1+\nu^{M})\left[(1+\sqrt{\rho})\nu^{M} - 2\nu^{M}\right]}. \tag{7}$$

Importantly, Eq. 6 allows for the calculation of the Young's modulus of the matrix E^{M} from the actual strain and thermal strain of the circle, ε and ε_{T}, respectively. As we do not know the precise values of of ν^{M} and ρ^{M}, we report the apparent modulus of the matrix as the product $E^{M}g(\nu,\rho)$.

Experiments with Cells and Stiff Inclusions

Cell Culture and Matrix Preparation

Experiments were conducted using the migratory human breast cancer cell line MDA-MB-231. The cells were maintained in Dulbecco's modified Eagle's medium (Corning) with 10% fetal bovine serum (Corning) in an incubator at 37°C and 5% CO_2. Cell spheroids were formed using a 3D Petri dish mold (MicroTissues, Inc.) to have an average radius of 300 μm, which was the largest size that could be produced. Stiff inclusions were either 3.5 mm diameter poly(methyl methacrylate) (PMMA) spheres or poly(dimethylsiloxane) (PDMS) rectangles of 9 mm length, 2 mm width, and 1 mm height. Both PMMA and PDMS were several orders of magnitude stiffer than cells and collagen matrix. The PDMS rectangles were treated using poly(ethyleneimine) and glutaraldehyde, to make them adhere covalently to collagen fibers. The PMMA spheres adhered covalently to collagen fibers with no treatment required. A thick ($\approx$ 2 mm) gel of rat tail collagen I (Corning) with final concentration 3 mg/mL was polymerized at 32°C at the bottom of a glass bottom dish. The glass bottom dish was previously treated with glutaraldehyde so that the collagen gel would adhere to it. A cell spheroid and a stiff inclusion were placed on the gel separated by distances ranging from 0.5–3 mm. Then, a second 3 mg/mL collagen layer was polymerized at the same temperature on top of the first with one. The overall thickness of the two-layered gel was 4–6 mm. Cell medium was then added to the dish. Following our previous studies that measured fiber length in collagen matrices,[31] we estimated the average fiber length in these collagen gels to be $l_{f} \approx 8$ μm, giving a ratio of cell spheroid radius to fiber length of $R/l_{f} \approx 40$.

Microscopy and Image Analysis

Once the gels were polymerized, images were collected using a Ti-E microscope and a $10\times$ numerical aperture 0.25 air objective in phase contrast mode running Elements Ar software (all Nikon). A 16×16 grid of images was collected and stitched together using Elements Ar software. After image collection, the gels were maintained in a cell culture incubator for 96 hours. The cell culture medium was replaced 36 hr after gel polymerization. At 96 hr after polymerization, images of the whole dish area were again collected on the microscope.

The images were analyzed using ImageJ and Adobe Illustrator to measure areas of spheroid spreading toward and away from the stiff inclusion due to cell migration. Starting with an image collected immediately after polymerizing the gel, a line was drawn from the spheroid centroid to the nearest point of the stiff inclusion, and its distance was measured. The same line was extended to the outer edge of the collagen gel and its distance was measured to identify the position of the spheroid centroid at time 0. A second line was drawn perpendicular to the first and passing through the centroid of the spheroid. This second line was then drawn on the image collected at the 96 hr time point, and it divided the cell spheroid into two. The distance between the spheroid centroid and the outer edge of the collagen gel remained constant, verifying that the gel did not expand or contract in the in-plane direction. Areas of spheroid spreading toward and away from the stiff inclusion were measured, and the ratio was computed. A ratio equal to one indicates no preference of cells migrating toward or away from the stiff inclusion, whereas a ratio larger than one indicates preferential migration toward the stiff inclusion.

Results and Discussion

To motivate our study, we began by imaging the complex structure of the ECM from real tissues. Fig. 1a shows an image of collagen fibers surrounding a duct in a murine mammary gland. The fibers have nominally isotropic orientation with no clear direction of alignment. Fig. 1b and c show cancer cells, collagen fibers, and stromal/immune cells in the early stages of a murine model of breast cancer. These images show matrices of varying fiber density embedded with tumors, which are stiffer than the surrounding tissue.[13,15,44] The matrices surrounding the tumors were nominally isotropic, with no distinct fiber alignment, which is typical of benign tissue and early stages in cancer.[15,32–34] Stromal cells (magenta) were located near to each large rigid tumor mass (cyan) and were physically connected to it through attached collagen fibers. If a cell some distance from a tumor were to contract, force propagation through the matrix would potentially cause the cell to sense a stiffer local environment. Similarly, because the tumor mass can contract against the fibers, cells within one tumor could potentially sense increased stiffness caused by another tumor some distance away. However, the extent to which matrix heterogeneity disrupts this potential for cell sensing of locally stiff features in the matrix remains unknown.

To determine how a contracting cell could potentially sense a stiff inclusion some distance away, we designed experiments to induce local contraction near to a stiff inclusion in a fibrous collagen gel. The collagen fiber orientation was random, representative of benign tissue and early stages of disease. A contractile PNIPAAm particle of radius R was located a distance d from the stiff inclusion (Fig. 2a), and, upon heating, it produced a contractile displacement field in the collagen gel (Fig. 2b). To analyze the displacements, we plotted the inward radial component of displacement $-u_r$ against the radial distance from the center of the particle r for several different paths drawn outward from the contracting particle (Fig. 2c). Lines colored

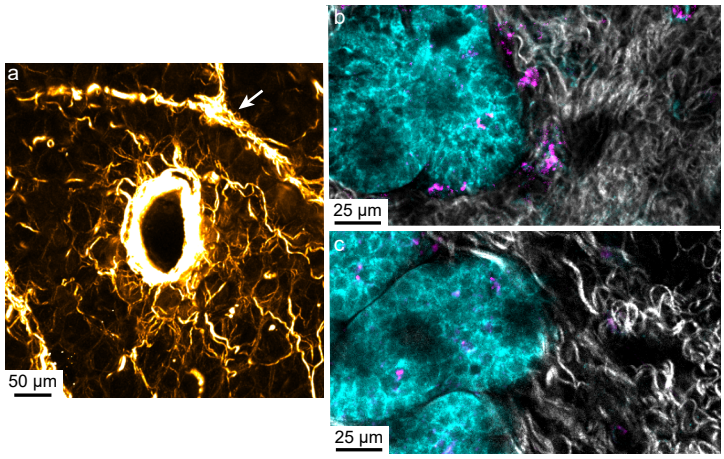

Figure 1: Representative images of ECM near to heterogeneous matrix features in murine mammary glands. (a) Image of collagen fibers (yellow) having random orientation surrounding a duct (white oval) in benign tissue. The arrow points to a blood vessel. (b, c) Images of collagen fibers (gray) next to early stage mouse mammary tumors (cyan). Stromal cells and macrophages are shown in magenta. The images illustrate regions of high (b) and low (c) fiber density.

in red and blue indicate displacements towards and away from the stiff inclusion, respectively, as illustrated in Fig. 2a. To quantify how the displacement field decayed over space, we initially fit to a function of the form $u_r = -Ar^{-n_1} + Br^{n_2}$ but found that the magnitude of A was orders of magnitude larger than B, which motivated a simpler fitting, $u_r = -Ar^{-n}$. This fitting was used in prior studies, which used n to quantify the rate of decay of displacements over space.[18,20] Although the value of n for directions away from and towards the stiff inclusion appeared different, there was notable variability resulting from randomness in the fiber structure (Fig. 2d).

To account for the variability while comparing displacements in the different directions, a 95% confidence interval was computed for the ratio of decay rates n in directions away from and toward the inclusion. The confidence interval, [0.70, 1.7], spanned unity, indicating that the value of n was affected more so by randomness in the fiber structure than by the presence of the inclusion. To analyze results for multiple particles, 95% confidence intervals were computed and plotted against dimensionless distance d/R between particle and inclusion (Fig. 2e). Most confidence intervals spanned unity, including for d/R as small as 2.5, indicating that the corresponding displacement fields were not statistically affected by the presence of the stiff inclusion. However, some confidence intervals remained below one, including for the greatest dimensionless distance of $d/R = 5.8$. Hence, there was no clear relationship between distance d/R and the effect of the stiff inclusion on the displacement field, which suggests that the random fibrous structure may have a larger effect on the displacement fields than the proximity to the stiff inclusion.

The stiff inclusion of Fig. 2 was similar to a symmetric boundary, which motivated us to perform additional experiments with symmetric pairs of contracting particles. Because the distance between the two particles was double the distance between a particle and symmetric boundary, we defined the distance between the particles to be $2d$ (Fig. 3a). As before, the displacement field induced by each contracting particle was measured (Fig. 3b), and the decay rate of the displacements n was computed in directions away from and toward each particle's neighbor (Fig. 3c, d). Again, 95% confidence intervals of the ratio of n in

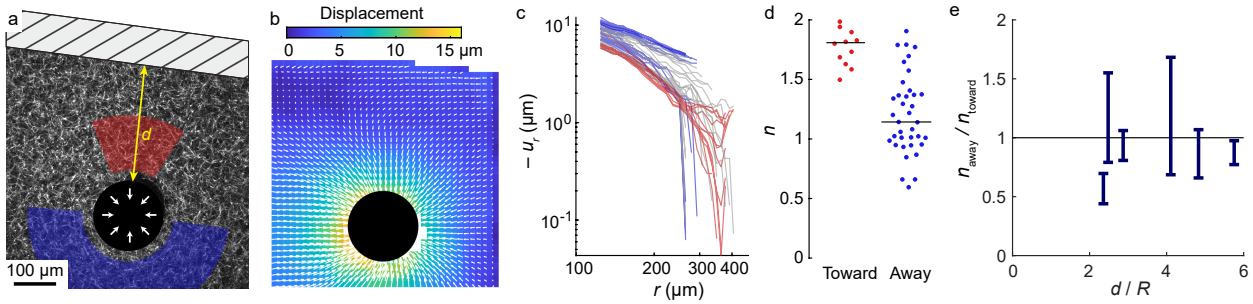

Figure 2: Displacement field induced by a contracting particle near a stiff inclusion. (a) Representative image from experiments showing the particle (black) and inclusion (cross-hatched). Regions highlighted in red and blue show directions defined as toward and away from the inclusion, respectively. (b) Displacement field induced by the contracting particle. (c) Inward radial component of displacement $-u_r$ plotted against distance from the center of the particle r for different paths drawn outward from the particle center. Lines are color coded such that red and blue indicate directions toward and away from the inclusion (defined in panel a); gray indicates directions that are unshaded in panel a. (d) Decay rate n from fitting displacements in panel c to $u_r = -Ar^{-n}$ for directions toward and away from the inclusion. The 95% confidence interval of the ratio of n in directions away from and toward the inclusion is [0.70, 1.7]. (e) 95% confidence intervals for the ratio of n away from and toward the inclusion for multiple different contracting particles at multiple dimensionless distances d/R from the inclusion.

directions away from and toward the neighboring particle were calculated. For comparison, the confidence intervals from Fig. 2e were also included in the graph. Again, the majority of the confidence intervals spanned unity (Fig. 3e). The displacement field of one particle was only affected by the neighboring particle for short distances of $d/R < 2$, which is equivalent to < 1 particle diameter.

Although the data in Fig. 3e indicated altered displacement fields for the two pairs of particles separated by the smallest distances d/R, it could be that that the altered displacements were caused more so by the fiber structure, wherein the fibers happened to be randomly organized in a way that caused different decay of displacements in directions toward and away. Investigating this idea would require repeated experiments in different networks having the exact same network structure but different distances between particle and stiff inclusion. As such an experiment is not possible, we turned to a fiber network model. To match the boundary conditions of the experiments, the model included a contracting circle of radius R and a stiff inclusion located a distance d from the contracting circle. As in the experiments, the ratio of contracting circle radius and fiber length was $R/l_f = 2$. Representative displacement fields and curves of radial displacement vs. distance are given in Fig. 4a, b. As in the experiments, the displacement decay rate n was computed in directions away from and toward the stiff inclusion. For five different fiber networks, 95% confidence intervals were computed for d/R ranging from 0.5 to 4, as were confidence intervals in fiber networks with no stiff inclusion. The confidence intervals lacked discernible trends when plotted against dimensionless distance d/R (Fig. 4c). Additionally, some fiber networks had confidence intervals lower than unity for most distances whereas other fiber networks had confidence intervals that spanned unity for all distances (Fig. 4c). Together, these observations suggest that the structure of the fiber network near to the particle has a larger effect than distance to a stiff inclusion on the propagation of displacements.

In summary, Figs. 2–4 indicate that the displacement field of the contracting particle may have been altered by a stiff inclusion or a nearby contracting particle for short distances but that the structure of the fiber network seemed to have a dominant effect on the displacement fields. This finding adds more detail to

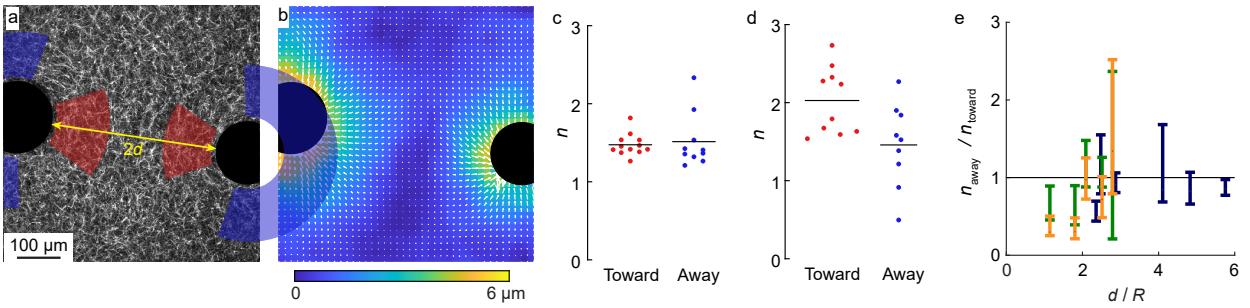

Figure 3: Displacement fields induced by pairs of contracting particles. (a) Experimental image with particles located a distance $2d$ from each other. Red and blue regions near each particle define directions toward and away from the other particle. (b) Displacement field induced by the particles in panel a. (c, d) Displacement decay rate n in directions toward and away for the particle on the left (c) and right (d). (e) 95% confidence intervals for different pairs of particles (green and yellow) located different distances from each other. Data from Fig. 2e are also included on this graph in blue.

prior literature demonstrating that stress and displacement fields propagate heterogeneously through fibrous materials.[30,31] In our experiments, the ratio of contracting particle radius to fiber length R/l_f was approximately 2, as described in Methods. Hence, the data suggest that a cell of size $2R$ contracting in a fibrous matrix with a ratio of cell radius to fiber length equal to 2 may sense the randomness of the matrix itself more so than the presence of stiff or compliant inclusions.

Until this point, the experiments and simulations have analyzed displacements, but stiffness is the property that is typically attributed to cell sensing and is used to characterize heterogeneous materials. Therefore, we combined the fiber network model with Eq. 6 to quantify the apparent modulus of the matrix sensed by contracting circles in the five different fiber networks of low fiber density (Fig. 5a). For a single network (identified by a single color in the figure), as the distance between the contracting circle and stiff inclusion d/R was reduced, the apparent modulus increased by $\sim$50%, indicating a gradient in stiffness toward the stiff inclusion. Between different fiber networks, there was notable heterogeneity, with a factor of $\sim$2 variability in apparent modulus. Hence, although the stiff inclusion created a stiffness gradient, its magnitude was relatively small compared to the heterogeneity caused by the random structure of the fibers. Following prior research demonstrating that nonlinearity of fibrous materials causes nonaffine and heterogeneous displacements to become less pronounced at larger strain,[45,46] we repeated the simulations with large contractile strains of 15% and 30% (Fig. 5b, c), expecting to see reduced network-to-network variability. The strains of 15% and 30% produced nonlinearity, as indicated by the increase in stiffness observed at increased strain. To our surprise, however, the reduction in variability was modest, with the stiffness sensed by contracting circles in different fiber networks still varying by nearly 50% for the largest strain. Although surprising, this observation was consistent with the experimental data, wherein contractile strains were in the range of 10–20%, and the displacement fields were rarely affected by the presence of a stiff inclusion (Figs. 2–3). Together, these results suggest that a stiff inclusion could sometimes produce a clear gradient in stiffness, but more commonly the gradient would be masked by heterogeneity caused by the random structure of the fibers.

To rule out that our results were affected by the specific type of loading produced by the contracting circle, we repeated the simulations using a contracting force dipole, which may better match the contractile

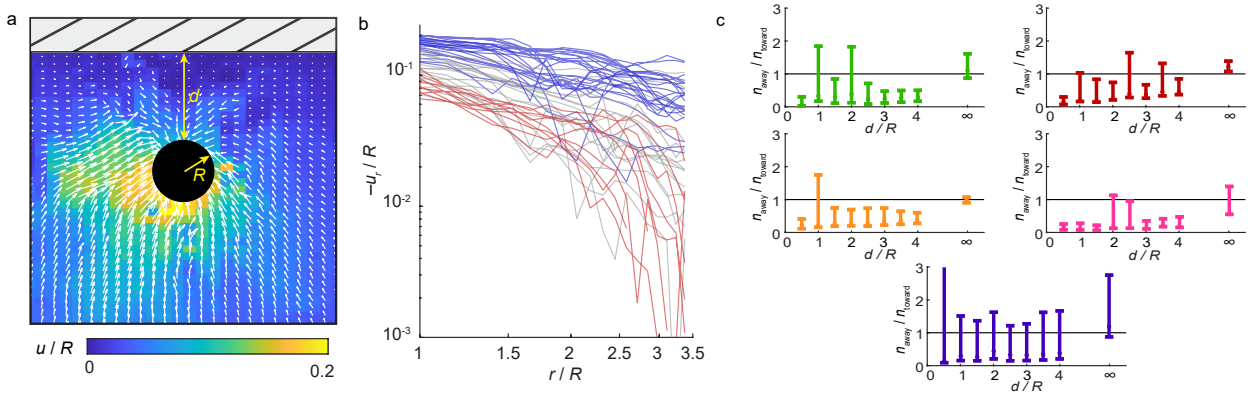

Figure 4: Displacement fields in fiber network model. (a) Representative displacement field of a particle of radius R (black) located a distance d from a stiff inclusion (cross-hatched). Displacements u are made dimensionless by normalizing by R. (b) Dimensionless inward radial displacement $-u_r/R$ plotted against distance from the center of the contracting particle. Blue and red indicate directions away from and toward the stiff inclusion; gray indicates directions neither towards nor away. (c) 95% confidence intervals of the ratio of decay rate n in directions away from and toward the inclusion for different dimensionless distances d/R. Each graph corresponds to a different fiber network.

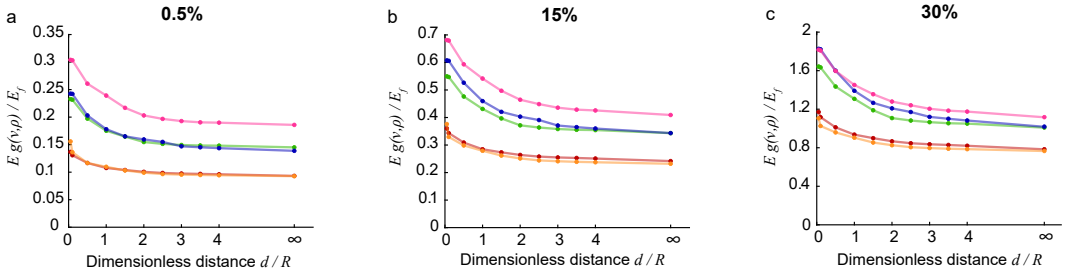

Figure 5: Apparent modulus sensed by a contracting circle of radius R in fiber networks with $R/l_f = 2$ with stiff inclusions located a dimensionless distance d/R away for (a) 0.5%, (b) 15% and (c) 30% contractile strain. Infinite distance corresponds to the case of no stiff inclusion. Each color indicates a different fiber network. Apparent modulus was made dimensionless by dividing by the fiber modulus E_f.

forces of a cell and was not testable experimentally using the spherical PNIPAAm particles. The dipole size was $2R$, the ratio R/l_f was equal to 2, and a stiff inclusion was positioned at distance d from the dipole. Simulations were run with the dipole oriented both parallel and perpendicular to the boundary of the stiff inclusion (Fig. 6a, b). As the results in Fig. 5 showed that the magnitude of contraction had only a modest effect on the apparent stiffness, the simulations with the dipole used only 0.5% and 15% contraction, because larger deformations were computationally expensive. As Eq. 6 applies for a contracting circle but not a dipole, we present the data as a dimensionless stiffness defined as the dimensionless ratio of force and displacement of the dipole, as described in Methods. For dipoles aligned both parallel (Fig. 6c, d) and perpendicular (Fig. 6e, f) to the stiff inclusion, effects of network-to-network heterogeneity were large compared to the increase in stiffness caused by the inclusion. In fact, network-to-network heterogeneity was larger for the dipoles than for the contracting circles, likely because the dipole applied force to only two points, resulting in a more concentrated loading than the contracting circle. Only for the parallel dipole at

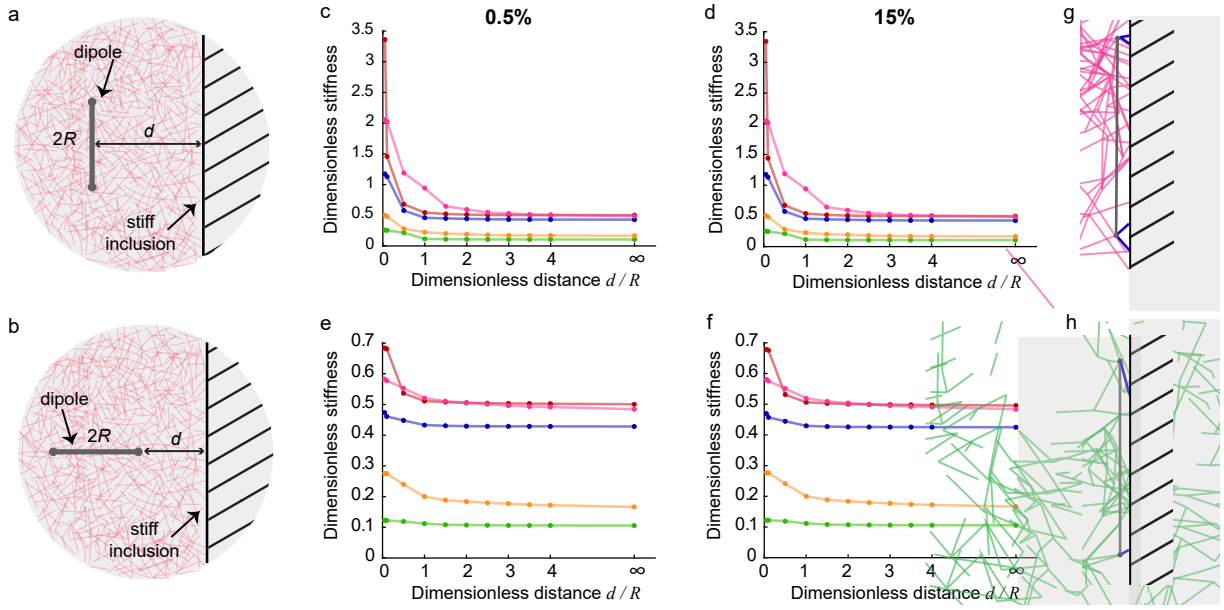

Figure 6: Apparent stiffness sensed by contracting dipoles of length $2R$ in fiber networks with $R/l_f = 2$ and stiff inclusions. (a, b) Schematics of contracting dipoles of length $2R$ located at distance d from stiff inclusions in the fiber network oriented parallel (a) and perpendicular (b) to the inclusions. (c, d) Apparent stiffness sensed by contracting dipoles parallel to stiff inclusions in five different fiber networks for two contractile strains, 0.5% (c) and 15% (d). (e, f) Apparent stiffness sensed by contracting dipoles perpendicular to stiff inclusions in five different fiber networks for two contractile strains, 0.5% (e) and 15% (f). Infinite distance corresponds to the case of no stiff inclusion. Each color indicates a different fiber network. (g, h) Zoomed-in images of the fiber networks colored pink (g) and green (h) that were used in Fig.9 c, d for simulations with a parallel dipole. The parallel dipole is shown in gray, and the stiff inclusion is the cross-hatched region. Fibers that connect directly from the dipole to the stiff inclusion are highlighted in blue. The dipole located in the pink network (g) was connected directly to the stiff inclusion through 4 fibers, while the dipole in the green network (h) was connected directly with the stiff inclusion through only 2 fibers.

very short distance (e.g., $d/R < 0.5$) was the effect of the stiff inclusion noticeable. The increase in stiffness at small d/R varied greatly for different fiber networks, with some networks (e.g., pink and red lines in Fig. 6c, d) showing dramatic stiffening whereas other (e.g., orange and green) showing only modest stiffening. The cause of this difference appeared to be that networks with large stiffening had more fibers connecting directly to the stiff inclusion as compared to the networks with minimal stiffening (Fig. 6g, h). In sum, the data from the contracting dipoles were consistent with our prior observations, namely that the increase in stiffness due to a stiff inclusion was typically smaller than the heterogeneity resulting from the randomness of the fiber network. Additionally, when the inclusion caused a large increase in stiffness, the increased stiffness depended on the precise details of the organization of fibers between the contracting dipole and the stiff inclusion (Fig. 6g), which emphasizes the large effect that the random structure of the fibers has on the stiffness.

Until now, the experiments and simulations have considered contraction in a fibrous matrix at length scales similar to the fiber length, specifically $R/l_f \approx 2$. As the quantity R/l_f is dimensionless, our findings can be applied broadly to any conditions for which contractile loads are applied at the scale $R/l_f \approx 2$. In prior studies,[8,20] we measured average fiber lengths in the range of 4 to 40 μm, suggesting that the stiffness

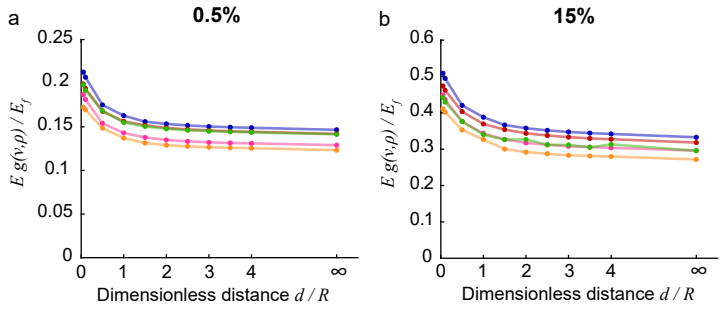

Figure 7: Apparent modulus sensed by a contracting circle of radius R in fiber networks with $R/l_f = 10$ and a stiff inclusion located a dimensionless distance d/R away for (a) 0.5% and (b) 15%. Infinite distance corresponds to the case of no stiff inclusion. Each color indicates a different fiber network. Apparent modulus was made dimensionless by dividing by the fiber modulus E_f.

sensed by contraction could be affected predominantly by network randomness on scales ranging from 8 to 80 μm, depending on the average fiber length. At smaller length scales, the stiffness would likely be even more subject to randomness, but because effects of randomness are reduced as either the average fiber length is decreased[8,31,36] or the size of the loading is increased,[47,48] it might be possible for a cue from a stiff inclusion to propagate over space in matrices having larger R/l_f, corresponding to matrices having short fibers and/or large contracting inclusions.

To test this prediction, we increased the size of the contracting circle by a factor of 5, giving $R/l_f = 10$ and repeated the simulations of the contracting circle of radius R located a distance d away from a stiff inclusion. As in the prior results, the apparent modulus increased with decreasing distance between the contracting circles and stiff inclusions (Fig. 7). In agreement with our expectation, the network-to-network variability was reduced such that apparent modulus varied by $\sim$20% between the different fiber networks for all applied strains. This variability was smaller than the 42% and 51% increase in apparent modulus that occurred at small d/R for 0.5% and 15% contraction, respectively, suggesting that a stiff inclusion would create a clear gradient in stiffness. These results indicate that as the size of the contracting inclusion is increased or the fiber length is decreased, variability between networks decreases leading to a gradient in stiffness.

To consider another means to reduce variability between different networks, we also generated fiber networks having high fiber density, double the density used previously. We repeated the simulations of contracting circles in fiber networks having R/l_f matching both values used in prior simulations, namely $R/l_f = 2$ and 10. For the networks with $R/l_f = 2$ the network-to-network variability in apparent modulus was $\sim$26% for all applied strains whereas the apparent modulus was increased by $\sim$61% at small d/R (Fig. 8a, b). For $R/l_f = 10$, the variability between different networks was $< 10\%$ for all applied strains, which was was far smaller than the 43% and 51% increase in apparent modulus that occurred at small d/R for 0.5% and 15% contraction, respectively (Fig. 8c, d). As expected, this last case of large inclusions in networks of high fiber density produced the smallest heterogeneity between different networks. As in Fig. 7, with heterogeneity reduced, a clear gradient in stiffness became apparent. A natural prediction is then that a large cellular structure, such as a multicellular spheroid, could sense such a gradient, enabling cells to migrate up the stiffness gradient, toward the stiff inclusion, similar to prior observations of durotaxis.[1]

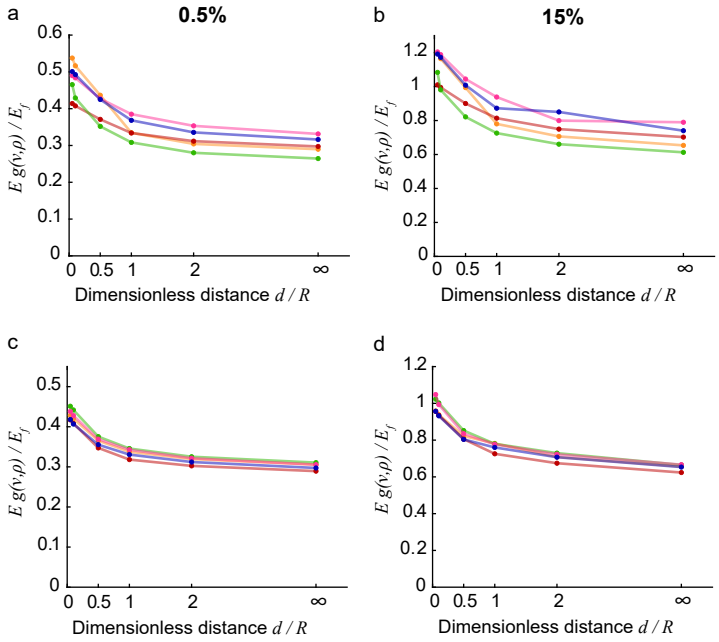

Figure 8: Apparent modulus sensed by a contracting circle in fiber networks of high fiber density with (a, b) $R/l_f = 2$ and (c, d) $R/l_f = 10$ and a stiff inclusion located a dimensionless distance d/R away. Results are shown for (a, c) 0.5% and (b, d) 15% contractile strain. Infinite distance corresponds to the case of no stiff inclusion. Each color represents a different fiber network. Apparent modulus was made dimensionless by dividing by the fiber modulus E_f.

To test for durotaxis caused by a stiff inclusion in a fibrous matrix, we designed experiments with spheroids of MDA-MB-231 cells fully embedded in collagen gels having stiff inclusions. As described in Methods, the estimated ratio of spheroid size to fiber length was $R/l_f \approx 40$. Stiff inclusions (either PMMA spheres or PDMS rectangles) were located a distance d from the cell spheroids, as shown in Fig. 9a. Our expectation was that the stiff inclusions would create gradients in stiffness, similar to the gradients observed in our model. In turn, durotaxis would imply that cells would migrate up the gradient, toward the stiff inclusion. Of course, our model did not match perfectly to these experiments, because it considered contraction of circles and dipoles, rather than the precise details of the forces of cell migration, but we reasoned that the model was useful as follows. For early time points, the spheroid was approximately spherically symmetric, and the contractile forces of each cell would be transmitted through the spheroid such that the overall contraction would occur on length scales approximately equal to the size of the spheroid, meaning the length scale R/l_f can reasonably be thought of as the ratio of spheroid radius to fiber length. At the same time, cells located on the side of the spheroid proximal to the stiff inclusion would sense greater stiffness than cells on the lateral sides. In turn, cells on the lateral sides would sense greater stiffness than cells on the side opposite to the stiff inclusion. Hence, the stiff inclusion could create a gradient in stiffness across the spheroid. Following durotaxis, cells would migrate into the surrounding matrix in the direction of the gradient, toward the stiff inclusion, causing the spheroid to spread preferentially in the direction of the stiff inclusion.

For each spheroid, an image was acquired upon embedding it in the collagen gel, from which the distance

d and spheroid radius R were measured. After 96 hr of cell spreading, an additional image was acquired and used to compute the area of spheroid spreading toward and away from the stiff inclusion (Fig. 9b–d). A ratio equal to 1 indicates no preference of cells migrating towards or away from the stiff inclusion, whereas a ratio larger than 1 indicates preferential migration towards the stiff inclusion. When plotted against dimensionless distance d/R, the spreading ratios appeared to be larger than 1 for small d/R but not for large d/R (Fig. 9e, f). We considered that for large d/R, some spheroids may have been closer to the edge of the collagen gel than to the stiff inclusion, which could have caused a confounding effect. To investigate this possibility, we identified all spheroids from Fig. 9e & f for which the distance to the edge of the matrix was smaller than the distance to the stiff inclusion and graphed the resulting data set (Fig. 9g). A statistical test demonstrated that the area ratios were not statistically different from 1, suggesting no confounding effect caused by the edge of the matrix. Next, the data for PDMS and PMMA inclusions were binned into two groups separated by the arbitrarily chosen dimensionless distance between spheroid and inclusion of $d/R = 3$. For $d/R > 3$, the data were not statistically different from 1, indicating random migration, but for $d/R < 3$ the data were statistically different from 1, indicating directional cell migration in response to the stiff inclusions (Fig. 9h, i). This observation held for both types of stiff inclusion, sphere and rectangle, though the data with the rectangle were smoother, likely because the rectangles were larger, thus creating smoother gradients in stiffness. These experimental data, together with the model results, indicate that stiffness sensing over a distance in a fibrous matrix requires a large ratio of cell size to fiber length. Such a large ratio occurs in clusters of cells, as in the tumors shown in Fig. 1. Hence, even in nominally isotropic matrices typical of early stages in cancer, the cancer cells could sense an environment having increased stiffness, which could further promote cancerous phenotypes.

Conclusions

Motivated by the complex and random structure of the extracellular matrix *in vivo*, our objective was to determine the extent to which matrix heterogeneity disrupts the potential for cell sensing of a locally stiff inclusion in a nominally isotropic matrix. To answer this question, it was necessary to compare the relative effects of the stiff inclusion and heterogeneity due to randomness in the local fiber structure. Using a combination of experiments and simulations, we found that, at the scale of a single cell, the random fibrous structure produced large spatial heterogeneities in stiffness. As a result, variability in stiffness was typically larger than the increase in stiffness caused by a stiff inclusion, even when the distance between the contracting unit and stiff inclusion approached zero. This result was affected only modestly by increasing the magnitude of contraction or by changing the loading conditions from a contracting circle to a contracting dipole. The picture that results from these observations is one wherein gradients in stiffness caused by stiff matrix features are typically no larger than gradients due to matrix heterogeneity. Hence, a cell's durotactic response would depend on the precise structure of the nearby matrix fibers. For a cell to potentially sense a stiff region, the effect of heterogeneity would have to be reduced, either due to a large cell size or a short fiber length. In agreement with this interpretation, cell spheroids spreading in 3D collagen gels with a large ratio of cell size to fiber length showed preferential migration toward stiff inclusions.

Our findings emphasize the importance of length scale in a cell's ability to sense mechanical properties of the matrix. A multicellular tumor, having large size relative to the fiber length, would be relatively unaffected by matrix heterogeneity and could continuously sense distant stiff inclusions. By contrast, a single cell, being unable to spread to a sufficient size to average out the heterogeneity, would sense the stiffness of only

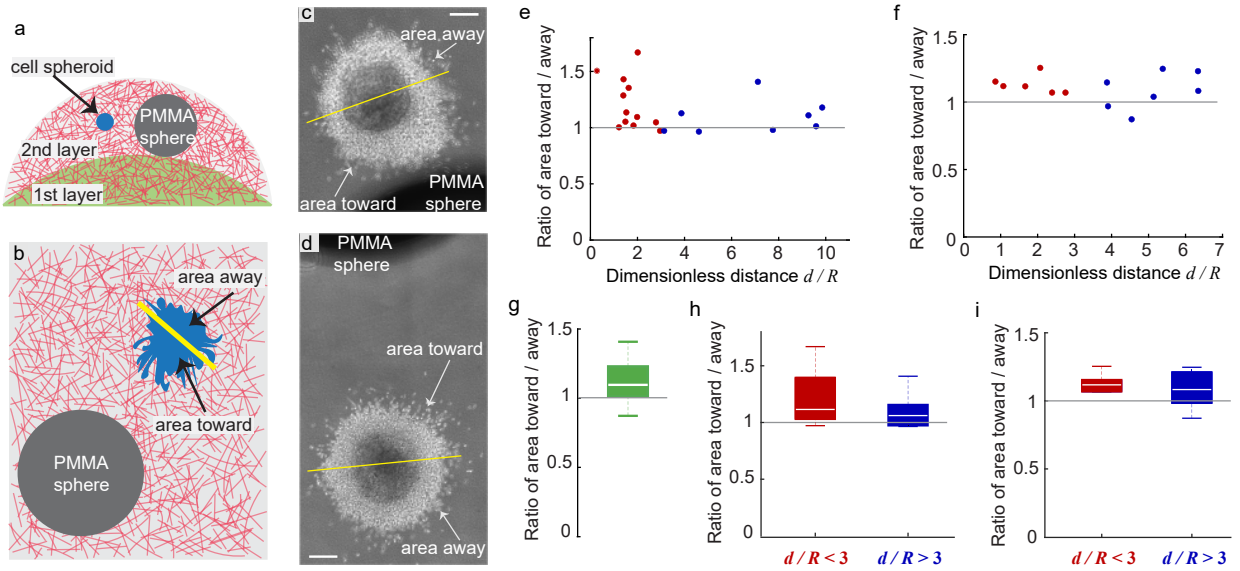

Figure 9: Spreading of cell spheroids near stiff inclusions in collagen gels. (a) Schematic of a cell spheroid of radius R and a PMMA sphere as the stiff inclusion embedded in a two-layered collagen gel. The distance between the edges of the spheroid and sphere is defined as d. (b) Schematic of a collagen gel with PMMA sphere 96 hr after gel polymerization. Areas of spheroid spreading toward and away from the PMMA sphere are shown. (c, d) Experimental images at the 96 hr time point showing cell spheroids at distances $d/R = 1.63$ (c) and 4.61 (d) from PMMA spheres. Areas of spheroid spreading toward and away from the PMMA spheres are indicated. The ratios of areas are 1.35 and 0.96 for panels c and d, respectively. Scale bars: 250 μm. (e, f) Ratio of areas of spheroid spreading toward and away from PMMA spheres (e) and PDMS rectangles (f) plotted against dimensionless distance d/R from the stiff inclusion. Each dot represents one cell spheroid. Dots in red and blue represent ratios of areas of cell spheroids located at $d/R < 3$ and $d/R > 3$, respectively. (g) Box plot of area ratios of spheroids that were closer to the edge of the gel than to the stiff inclusion (PDMS or PMMA). Data are not statistically different from 1 ($p = 0.11$, sign test). (h, i) Box plots of area ratios for spheroids embedded in matrices with PMMA spheres (h) and PDMS rectangles (i). For both panels, spheroids for which $d/R < 3$ (red) had area ratios significantly greater than 1 ($p = 0.01$ and 0.03 for panels g and h, respectively, sign test), and spheroids for which $d/R > 3$ (blue) had area ratios that were not significantly different from 1 ($p = 0.73$ and 0.45, sign test).

the nearby fibers. That local stiffness would vary between large and small values, depending on the cell's exact location in space. In this way, the heterogeneity typical of normal, nominally isotropic matrices shields the cell from distant mechanical cues, which raises the possibility that the mechanical heterogeneity present in normal matrix contributes to maintenance of homeostatic conditions.

Conflicts of Interest

There are no conflicts to declare.

Acknowledgments

We thank Mainak Sarkar for technical discussions and David Inman for assistance with preparing the animal tissue. We acknowledge the University of Wisconsin Translational Research Initiatives in Pathology laboratory for use of the vibratome. This work was supported by National Science Foundation grant number CMMI-1749400 and by the National Cancer Institute of the National Institutes of Health under award num-

bers R01CA216248, R01CA179556, and University of Wisconsin Carbone Cancer Center Support Grant P30CA014520.

References

[1] C. M. Lo, H. B. Wang, M. Dembo and Y. L. Wang, *Biophys J*, 2000, **79**, 144–152.

[2] C. A. Reinhart-King, M. Dembo and D. A. Hammer, *Biophys J*, 2008, **95**, 6044–6051.

[3] P. P. Provenzano, D. R. Inman, K. W. Eliceiri and P. J. Keely, *Oncogene*, 2009, **28**, 4326–4343.

[4] X. Tang, P. Bajaj, R. Bashir and T. A. Saif, *Soft Matter*, 2011, **7**, 6151–6158.

[5] M. A. Kotlarchyk, S. G. Shreim, M. B. Alvarez-Elizondo, L. C. Estrada, R. Singh, L. Valdevit, E. Kniazeva, E. Gratton, A. J. Putnam and E. L. Botvinick, *Plos One*, 2011, **6**, e20201.

[6] C. A. Jones, M. Cibula, J. Feng, E. A. Krnacik, D. H. McIntyre, H. Levine and B. Sun, *P Natl Acad Sci USA*, 2015, **112**, E5117–E5122.

[7] S. Van Helvert and P. Friedl, *ACS Appl Mater Inter*, 2016, **8**, 21946–21955.

[8] M. Proestaki, A. Ogren, B. Burkel and J. Notbohm, *Exp Mech*, 2019, **59**, 1323–1334.

[9] A. Hayn, T. Fischer and C. T. Mierke, *Front Cell Dev Biol*, 2020, **8**, 593879.

[10] M. Keating, A. Kurup, M. Alvarez-Elizondo, A. Levine and E. Botvinick, *Acta Biomater*, 2017, **57**, 304–312.

[11] Y. L. Han, P. Ronceray, G. Xu, A. Malandrino, R. D. Kamm, M. Lenz, C. P. Broedersz and M. Guo, *P Natl Acad Sci USA*, 2018, **115**, 4075–4080.

[12] F. Liu and D. J. Tschumperlin, *J Vis Exp*, 2011, e2911.

[13] J. I. Lopez, I. Kang, W.-K. You, D. M. McDonald and V. M. Weaver, *Integr Biol*, 2011, **3**, 910–921.

[14] A. J. Booth, R. Hadley, A. M. Cornett, A. A. Dreffs, S. A. Matthes, J. L. Tsui, K. Weiss, J. C. Horowitz, V. F. Fiore, T. H. Barker *et al.*, *Am J Resp Crit Care*, 2012, **186**, 866–876.

[15] I. Acerbi, L. Cassereau, I. Dean, Q. Shi, A. Au, C. Park, Y. Chen, J. Liphardt, E. Hwang and V. Weaver, *Integr Biol*, 2015, **7**, 1120–1134.

[16] V. F. Achterberg, L. Buscemi, H. Diekmann, J. Smith-Clerc, H. Schwengler, J.-J. Meister, H. Wenck, S. Gallinat and B. Hinz, *J Invest Dermatol*, 2014, **134**, 1862–1872.

[17] J. P. Winer, S. Oake and P. A. Janmey, *Plos One*, 2009, **4**, e6382.

[18] J. Notbohm, A. Lesman, P. Rosakis, D. A. Tirrell and G. Ravichandran, *J R Soc Interface*, 2015, **12**, 20150320.

[19] T. T. Falzone and R. M. Robertson-Anderson, *ACS Macro Lett*, 2015, **4**, 1194–1199.

[20] B. Burkel and J. Notbohm, *Soft Matter*, 2017, **13**, 5749–5758.

[21] M. S. Rudnicki, H. A. Cirka, M. Aghvami, E. A. Sander, Q. Wen and K. L. Billiar, *Biophys J*, 2013, **105**, 11–20.

[22] H. Mohammadi, P. A. Janmey and C. A. McCulloch, *Biomaterials*, 2014, **35**, 1138–1149.

[23] D. Stopak and A. K. Harris, *Dev Biol*, 1982, **90**, 383–398.

[24] D. Vader, A. Kabla, D. Weitz and L. Mahadevan, *Plos One*, 2009, **4**, e5902.

[25] S. Natan, Y. Koren, O. Shelah, S. Goren and A. Lesman, *Mol Biol Cell*, 2020, **31**, 1474–1485.

[26] R. S. Sopher, H. Tokash, S. Natan, M. Sharabi, O. Shelah, O. Tchaicheeyan and A. Lesman, *Biophys J*, 2018, **115**, 1357–1370.

[27] G. Grekas, M. Proestaki, P. Rosakis, J. Notbohm, C. Makridakis and G. Ravichandran, *J R Soc Interface*, 2021, **18**, 20200823.

[28] J. Kim, J. Feng, C. A. Jones, X. Mao, L. M. Sander, H. Levine and B. Sun, *Nat Comm*, 2017, **8**, 1–7.

[29] E. Ban, J. M. Franklin, S. Nam, L. R. Smith, H. Wang, R. G. Wells, O. Chaudhuri, J. T. Liphardt and V. B. Shenoy, *Biophys J*, 2018, **114**, 450–461.

[30] R. C. Arevalo, P. Kumar, J. S. Urbach and D. L. Blair, *Plos One*, 2015, **10**, e0118021.

[31] B. Burkel, M. Proestaki, S. Tyznik and J. Notbohm, *Phys Rev E*, 2018, **98**, 052410.

[32] P. P. Provenzano, K. W. Eliceiri, J. M. Campbell, D. R. Inman, J. G. White and P. J. Keely, *BMC Med*, 2006, **4**, 1–15.

[33] M. Egeblad, M. G. Rasch and V. M. Weaver, *Curr Opin Cell Biol*, 2010, **22**, 697–706.

[34] P. Schedin and P. J. Keely, *CSH Perspect Biol*, 2011, **3**, a003228.

[35] E. Bar-Kochba, J. Toyjanova, E. Andrews, K.-S. Kim and C. Franck, *Exp Mech*, 2015, **55**, 261–274.

[36] P. Grimmer and J. Notbohm, *J Biomech Eng*, 2018, **140**, 041011.

[37] S. B. Lindström, D. A. Vader, A. Kulachenko and D. A. Weitz, *Phys Rev E*, 2010, **82**, 051905.

[38] S. B. Lindström, A. Kulachenko, L. M. Jawerth and D. A. Vader, *Soft Matter*, 2013, **9**, 7302–7313.

[39] A. M. Stein, D. A. Vader, L. M. Jawerth, D. A. Weitz and L. M. Sander, *J Microsc*, 2008, **232**, 463–475.

[40] A. J. Licup, S. Münster, A. Sharma, M. Sheinman, L. M. Jawerth, B. Fabry, D. A. Weitz and F. C. MacKintosh, *P Natl Acad Sci USA*, 2015, **112**, 9573–9578.

[41] A. S. Van Oosten, M. Vahabi, A. J. Licup, A. Sharma, P. A. Galie, F. C. MacKintosh and P. A. Janmey, *Sci Rep*, 2016, **6**, 1–9.

[42] M. Vahabi, A. Sharma, A. J. Licup, A. S. Van Oosten, P. A. Galie, P. A. Janmey and F. C. MacKintosh, *Soft Matter*, 2016, **12**, 5050–5060.

[43] P. Rosakis, J. Notbohm and G. Ravichandran, *J Mech Phys Solids*, 2015, **85**, 18–32.

[44] K. R. Levental, H. Yu, L. Kass, J. N. Lakins, M. Egeblad, J. T. Erler, S. F. Fong, K. Csiszar, A. Giaccia, W. Weninger *et al.*, *Cell*, 2009, **139**, 891–906.

[45] P. Onck, T. Koeman, T. Van Dillen and E. van der Giessen, *Phys Rev Lett*, 2005, **95**, 178102.

[46] Q. Wen, A. Basu, J. P. Winer, A. Yodh and P. A. Janmey, *New J Phys*, 2007, **9**, 428.

[47] H. Hatami-Marbini and R. Picu, *Phys Rev E*, 2008, **77**, 062103.

[48] F. Beroz, L. M. Jawerth, S. Münster, D. A. Weitz, C. P. Broedersz and N. S. Wingreen, *Nat Comm*, 2017, **8**, 16096.